University of Groningen

Microglia morphotyping in the adult mouse CNS using hierarchical clustering on principal components reveals regional heterogeneity but no sexual dimorphism

van Weering, Hilmar R.J.; Nijboer, Tjalling W.; Brummer, Maaike L.; Boddeke, Erik W.G.M.; Eggen, Bart J.L.

[Link to publication in University of Groningen/UMCG research database](#)

RESEARCH ARTICLE

Microglia morphotyping in the adult mouse CNS using hierarchical clustering on principal components reveals regional heterogeneity but no sexual dimorphism

Hilmar R. J. van Weering | Tjalling W. Nijboer | Maaike L. Brummer |
Erik W. G. M. Boddeke | Bart J. L. Eggen

Department of Biomedical Sciences of Cells &
Systems, Section Molecular Neurobiology,
University Medical Center Groningen,
University of Groningen, Groningen,
The Netherlands

Correspondence
Bart J. L. Eggen, Department of Biomedical
Sciences of Cells & Systems, Section Molecular
Neurobiology, University Medical Center
Groningen, University of Groningen,
Groningen, The Netherlands.
Email: b.j.l.eggen@umcg.nl

Abstract

Microglia are the resident macrophages of the central nervous system (CNS) and play a pivotal role in immune surveillance and CNS homeostasis. Morphological transitions in microglia are indicative for local changes in the CNS microenvironment and serve as a proxy for the detection of alterations in the CNS, both in health and disease. Current strategies to 'measure' microglia combine advanced morphometrics with clustering approaches to identify and categorize microglia morphologies. However, these studies are labor intensive and clustering approaches are often subject to relevant feature selection bias. Here, we provide a morphometrics pipeline with user-friendly computational tools for image segmentation, automated feature extraction and morphological categorization of microglia by means of hierarchical clustering on principal components (HCPC) without the need for feature inclusion criteria. With this pipeline we provide new and detailed insights in the distribution of microglia morphotypes across sixteen CNS regions along the rostro-caudal axis of the adult C57BL/6J mouse CNS. Although regional variations in microglia morphologies were evident, we found no evidence for male–female dimorphism at any CNS region investigated, indicating that - by and large - microglia in adult male and female mice are morphometrically indistinguishable. Taken together, our newly developed pipeline provides valuable tools for objective and unbiased identification and categorization of microglia morphotypes and can be applied to any CNS (disease) model.

KEYWORDS
categorization, hierarchical clustering, microglia, morphology, morphometrics, PCA, principal component

1 | INTRODUCTION

Microglia are the tissue-resident macrophages of the central nervous system (CNS) and play a pivotal role in immune surveillance, CNS homeostasis maintenance and neuroinflammation. Research on microglia in recent years has benefited from improved microglia isolation protocols and rapidly evolving high throughput analyses. It is now evident that microglia are phenotypically diverse, and that subpopulations of microglia with distinct phenotypes are dynamically distributed throughout the CNS in a time- and space-dependent manner, both in

health and in disease (Bottcher et al., 2019; Grabert et al., 2016; Grabert & McColl, 2018; Masuda et al., 2019), discussed in (Eggen et al., 2019; Masuda et al., 2020; Paolicelli et al., 2022; Tan et al., 2020).

Microglia come in various shapes and sizes and their cellular distribution differs per brain region (Lawson et al., 1990). Under physiological conditions, microglia adapt a typically ramified morphology characterized by a small cell body and fine branched processes. By extension and retraction of these processes, microglia monitor the functional state of neuronal synapses and continuously scan their microenvironment for homeostatic disturbances (Davalos et al., 2005; Nimmerjahn et al., 2005; Wake et al., 2009). When challenged, microglia undergo a phenotypic shift, that is, they switch from a surveillant to a reactive state, a transitional process often accompanied by morphological changes. For example, microglia rapidly respond to local damage by directed extension of their processes to shield off the site of injury (Davalos et al., 2005; Nimmerjahn et al., 2005). In response to more extensive damage, microglia retract their processes and transform into amoeboid cells with proliferative, migratory and phagocytic properties (Kreutzberg, 1996). Thus, specific microglia morphotypes may reflect specific functional states. Morphological transitions in microglia are indicative for local changes in the CNS microenvironment and serve as a proxy for the detection of physiological and pathological alterations in the CNS.

Quantitative assessment of microglia morphologies in fixed tissues is commonly performed by morphometric analysis of digitally reconstructed cell silhouettes. Microglia are visualized by transgenic tagging or immunohistochemical staining for ionized calcium-binding adapter molecule 1 (IBA1), Integrin alpha M (ITGAM, CD11b) or EGF-like module containing mucin-like hormone receptor-like 1 (F4/80). Digital images of the stained tissues are subsequently processed and converted to binary images by means of threshold segmentation – thereby differentiating cell silhouettes from the background – and analyzed. The 'morphology' of a cell is determined by any given set of descriptors, ranging from area/perimeter measurements, branch (node) counts, form factors and ratio's to Sholl features (Sholl, 1953), fractal features (Karperien et al., 2013) and graph-based features (Colombo et al., 2022; Salamanca et al., 2019). However, defining microglia morphology based on morphometrics alone is inherently subject to feature selection bias. Moreover, any heterogeneity in microglia morphologies within experimental groups is readily overlooked when averaging group values.

In an attempt to more objectively identify and categorize microglia based on their morphology, current studies combine microglia morphometrics with clustering approaches (de Sousa et al., 2015; Fernandez-Arjona et al., 2017; Heindl et al., 2018; Ohgomori et al., 2016; Salamanca et al., 2019; Verdonk et al., 2016; Yamada & Jinno, 2013) or machine learning approaches (Leyh et al., 2021; Stetzik et al., 2022).

One way to morphologically define microglia subpopulations in a non-supervised manner is by means of hierarchical clustering of microglia based on a broad panel of morphometric features (de Sousa et al., 2015; Fernandez-Arjona et al., 2017; Ohgomori et al., 2016; Verdonk et al., 2016; Yamada & Jinno, 2013). One of the limitations of this approach is the requirement for the pre-selection of relevant features prior to clustering as morphometric datasets tend to be 'noisy' and redundant in features (Fernandez-Arjona et al., 2017; Heindl et al., 2018; Yamada & Jinno, 2013). Relevant feature selection prior to clustering can be effective when morphological differences or transitions in microglia are extensive and unidirectional – for example in inflammation -, but becomes challenging when experimental groups are heterogeneous and uniformly distributed, or when differences between groups are more subtle. Feature inclusion criteria based on bimodality coefficients such as the multimodality index (MMI >0.55, (Schweitzer & Renehan, 1997)) allow for pre-selection of 'relevant' morphometric features in rodent models for axotomy (Yamada & Jinno, 2013) and neuroinflammation (Fernandez-Arjona et al., 2017), but do not apply well to continuous datasets with unimodal distributed features (Soltys et al., 2005; also here).

Another approach to address noise and redundancy in a feature dataset is by reducing its dimensionality by means of a principal component analysis (PCA) (Gzielo et al., 2019; Heindl et al., 2018; Soltys et al., 2005). PCA is particularly useful in identifying highly correlating and thus redundant features (= features that contribute similarly to the variance in the dataset) as well as features that contribute uniquely to this variance. Principal components (PCs) generated by PCA may function as unique compound scores for microglia morphology as they represent linear combinations of the original features (Heindl et al., 2018). More interestingly, clustering on PCs instead of the original features should overcome the need for relevant feature selection allowing more objective and unbiased morphological categorization of microglia.

Microglia morphometric analyses are typically labor intensive and require dedicated imaging and analysis software systems. Secondly, whether clustering on PCs allows for morphological categorization of microglia has yet to be determined. This has prompted us to develop a pipeline with user-friendly computational tools for image extraction, image segmentation, automated morphometric feature extraction and morphological categorization of microglia by means of hierarchical clustering on principal components (HCPC). Digital slide scans of sagittal brain and spinal cord sections stained for IBA1 served as a starting point for our pipeline, which is divided into four steps; A. the extraction and archiving of single cell images from the digital slide scans at high resolution, B. the processing of the single cell images to trinary cell silhouette images, C. fully automated skeletonization and morphometric feature extraction, and D. an R-pipeline for in-depth data analysis and visualization, as well as HCPC-based categorization of microglia morphologies. Here, we used adult mouse C57BL/6J CNS tissue and defined sixteen gray, white and mixed matter regions along the rostral-caudal CNS axis for microglia density and detailed morphometrics analysis. Dimensionality reduction by PCA and subsequent hierarchical clustering of microglia based on PCs allowed for categorization of microglia morphologies without biased pre-selection of 'relevant' features. PCA and subsequent HCPC analysis revealed distinct heterogeneity in microglial morphotypes in and between CNS regions in the adult C57BL/6J CNS. Interestingly, no differences were observed in the relative number and distribution of microglial morphotypes between male and female littermates in any CNS region.
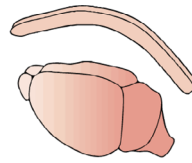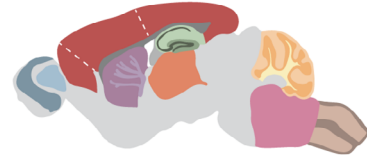

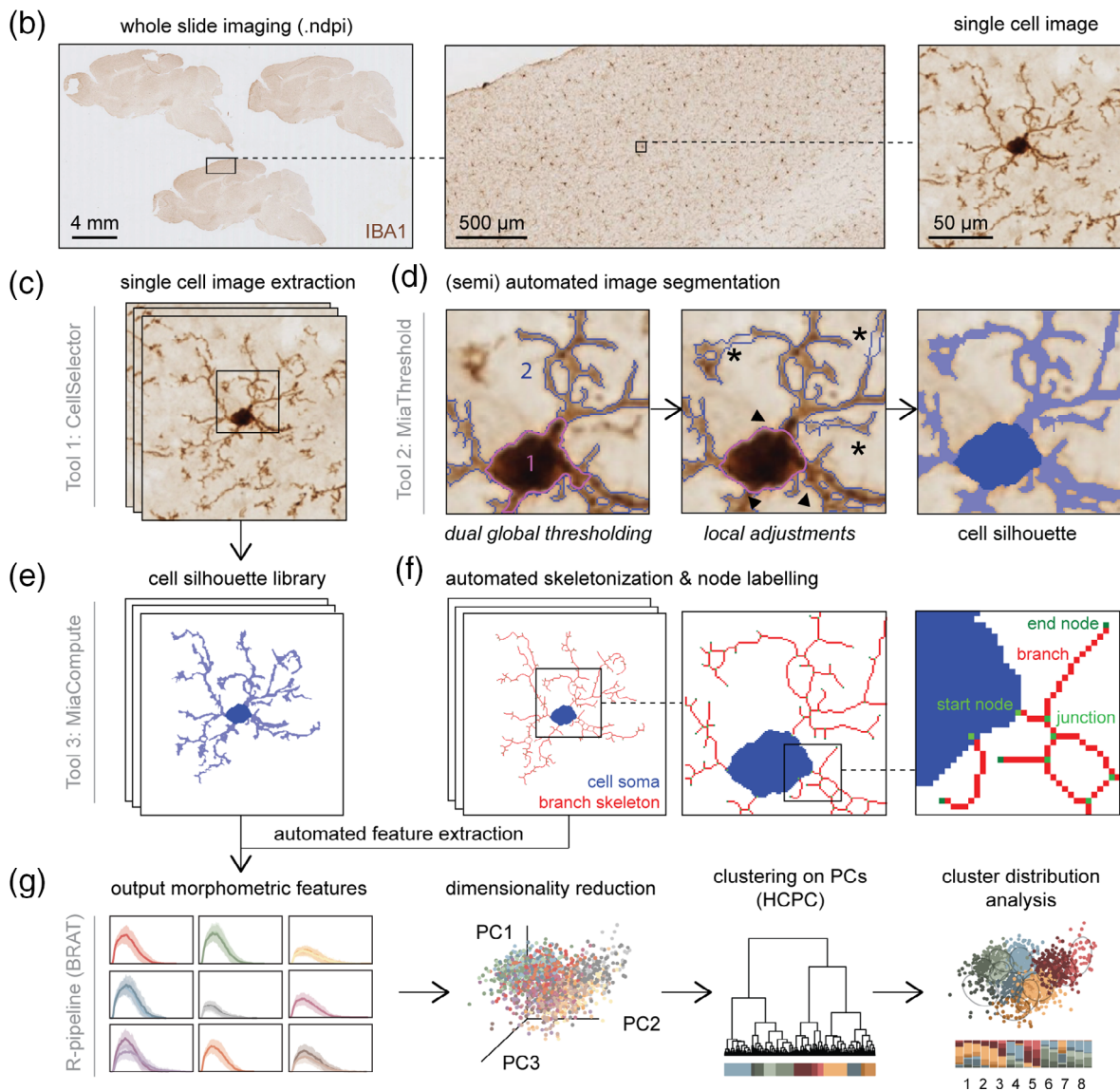

EXPERIMENTAL SET-UP
(a) C57BL/6J littermates (7♀/7♂)
perfusion
CNS isolation
(brain and spinal cord)
IBA1-IHC
microglia morphometrics and
cell density measurements in 16 CNS regions
OBg olfactory bulb, granule cell layer
OBp olfactory bulb, outer plexiform/glomerular layer
CPw caudate putamen, internal capsule tracts
CPg caudate putamen, grey matter
CA hippocampus, cornu ammonis
DG hippocampus, dentate gyrus
CC corpus callosum/ alveus fiber tracts
FIM fimbria
TH thalamus
CTX frontal isocortex, somatomotor areas 2/3/5
CBw cerebellum, arbor vitae
CBg cerebellum, granule cell layer
CBm cerebellum, molecular layer
MO medulla oblongata
SCw spinal cord C1-T13, (outer) white matter
SCg spinal cord C1-T13, grey matter
MORPHOMETRICS PIPELINE (b-g)
(b) whole slide imaging (.ndpi)
single cell image
4 mm
IBA1
500 µm
50 µm
(c) single cell image extraction
Tool 1: CellSelector
(d) (semi) automated image segmentation
Tool 2: MiaThreshold
2
1
*
*
*
dual global thresholding
local adjustments
cell silhouette
(e) cell silhouette library
Tool 3: MiaCompute
(f) automated skeletonization & node labelling
cell soma
branch skeleton
end node
branch
start node
junction
automated feature extraction
(g) output morphometric features
R-pipeline (BRAT)
dimensionality reduction
PC1
PC2
PC3
clustering on PCs
(HCPC)
cluster distribution
analysis
1 2 3 4 5 6 7 8

FIGURE 1 Legend on next page.

10981136, 2023, 10, Downloaded from https://onlinelibrary.wiley.com/doi/10.1002/glia.24427 by Universiteitsbibliotheek, Wiley Online Library on [19/09/2023]. See the Terms and Conditions (https://onlinelibrary.wiley.com/terms-and-conditions) on Wiley Online Library for rules of use; OA articles are governed by the applicable Creative Commons License

2 | MATERIALS AND METHODS

2.1 | Animals

Male and female C57BL/6J littermates (Jax® mouse strain) were housed on a 12-h day/light cycle with 2–3 animals per cage and ad libitum access to food and water. All experiments were performed in the central animal facility (CDP) of the UMCG and approved by the Institutional Animal Care and Use Committee (DEC-RUG) of the University of Groningen, protocol 15,360-03-007.

2.2 | Experimental set-up

An overview of the experimental set-up can be found in Figure 1a. Brains and spinal cords from 3-month-old male and female C57BL/6J littermates were isolated and processed for immunohistochemistry to visualize microglia (described in detail below). Microglia morphometrics and cell density measurements were applied in 16 specified regions following the rostro-caudal axis of the CNS; the granule cell layer (OBg) and outer plexiform/glomerular layer of the olfactory bulb (OBp), the caudate putamen (CPg) and internal capsule tracts into the caudate putamen (CPw), the frontal part of the somatomotor areas 2/3/5 of the isocortex (CTX), thalamus (TH), the cornu ammonis 1–3 (CA) and dentate gyrus (DG) of the hippocampus, the corpus callosum (CC), fimbria (FIM), the cerebellar molecular layer (CBm), cerebellar granule cell layer (CBg) and cerebellar arbor vitae (CBw), the medulla oblongata (MO) and the gray matter (SCg) and outer white matter (SCw) regions of the cervical/thoracic part of the spinal cord (Figure 1a). A schematic overview of the morphometrics and clustering pipeline can be found in Figure 1b–g and is described in detail below.

2.3 | Tissue isolation

Three-month old male and female C57BL/6J littermates ($n = 7$ per group) were terminated by deep anesthetization with isoflurane and subsequently perfused transcardially with phosphate-buffered saline (PBS, pH 7.4). Brains and spinal cords were rapidly isolated, collected in ice-cold PBS and fixed overnight in 4% paraformaldehyde (PFA) at 4°C. Tissues were stored at 4°C in PBS until they were processed for analysis.

2.4 | Tissue sectioning and immunohistochemistry

Prior to sectioning, the PFA-fixed tissues were dehydrated in 25% sucrose/PBS overnight (4°C) and embedded in O.C.T.™ compound (Tissue-Tek®) at −20°C. Series of sagittal sections of 16 μm thickness of both the brain and spinal cord tissues were prepared by cryosectioning. The sections were vacuum-dried for 30 min and post-fixed with 4% PFA for 10 min at room temperature (RT). Then, the sections were washed three times in PBS (which applies to all subsequent washing steps). Antigen retrieval was applied by placing the sections in 10 mM sodium citrate buffer (pH 6.0) and subsequent microwaving in a microwave steamer for 10 min at 1000 W.

Visualization of microglia was achieved by DAB-immunohistochemistry for ionized calcium-binding adapter molecule 1 (IBA1). In short, the sections were washed and incubated in 1% hydrogen peroxide (H_2O_2)/PBS for 10 min to block endogenous peroxidases (RT/in the dark). Subsequently, the sections were washed and pre-incubated in 5% normal goat serum (NGS; Vector laboratories, S-1000) in PBS supplemented with 0.3% Triton-X100 (PBS+) for 30 min at RT. After the pre-incubation step, the sections were incubated with rabbit-α-IBA1 (WAKO, 01–19,741; 1:1000) in 2%NGS/PBS+ overnight at 4°C. The following day, the sections were washed and incubated with biotinylated goat-α-rabbit IgG (Vector laboratories, BA-1000; 1:400) in PBS+ for 1 h at RT. After a washing step, the detection sensitivity of the antibodies was amplified by incubating in a VECTASTAIN® Elite® ABC-horse radish peroxidase working solution (Vector laboratories, PK-6100) for 30 min at RT. The sections were washed, and microglia were visualized by 0.4 mg/mL 3.3′-diaminobezidine/0.02% H_2O_2 in PBS. The staining reaction was stopped after approximately 5 min by rinsing the sections in demineralized water. The sections were subsequently dehydrated in graded ethanol series of 50–100%, air dried for 30 min and finally mounted with DePeX (Serva, 18,243) and a glass coverslip. The slides were stored at RT in the dark until further use.

2.5 | Digital slide scanning and image extraction

The sections were scanned at 40× magnification using a Nanozoomer 2HT 2.0 digital slide scanner system (Hamamatsu Photonics, K.K., Japan), resulting in whole slide scans at 0.227 μm/pixel resolution (Figure 1b). Extraction and archiving of single cell images was facilitated by *CellSelector* (Windows), a browser-based interface specifically developed for this purpose. *CellSelector* was written in Python 3.5 and

FIGURE 1 Overview experimental set-up and morphometrics pipeline. Schematic overview of the experimental set-up and CNS regions analyzed, with abbreviations (a) and the microglia morphometrics pipeline (b–g). (b) Digital images of a scan slide (left), magnification of a cortical region (middle) and magnification of a cortical microglial cell (right). (c) Single cell images extracted from the scans (tool 1: *CellSelector*) were submitted to (d) semi-automated image segmentation (tool 2: *MiaThreshold*). 1 indicates the initial soma threshold perimeter (in magenta), and 2 the branch perimeter (in blue). Asterisks indicate local adjustments to the branch perimeter, black arrows indicate local changes to the soma perimeter), generating (e) a cell silhouette library. Dark and light blue represent the soma and branches of the cell silhouette, respectively. The cell silhouette library served as input for (f) automated skeletonization, node labelling and subsequent feature extraction (tool 3: *MiaCompute*). (g) schematic overview of the bioinformatics pipeline (BRAT, R) for graphical output of the features (left), dimensionality reduction by PCA and subsequent morphological categorization of microglia by hierarchical clustering on principal components (HCPC, right). PC, principal component.

uses the OpenSlide 3.4.1, OpenSlide Python 1.1.1 (https://openslide. org/) and OpenSeadragon 2.4.0 (https://openseadragon.github.io/) libraries for reading and viewing of the digital slide scans (Figure 1c). The ndpisplit function of NDPITools (IMNC, Université Paris Sud) was used for the extraction and export of single cell .tiff images of 800 × 800 pixels. The .tiff files were subsequently converted to JPEG images using ImageMagick 7.0.8–24 (https://imagemagick.org). All cell coordinates were saved in *CellSelector* as metadata allowing tracking and tracing of previously selected cells.

The following criteria for cell selection were applied: 1. digital slide scans were user-blinded prior to cell selection, 2. cells were randomly selected per region, irrespective of their shape or size, 3. cells with apparent interruptions in the cell soma and/or branches as a result of tissue sectioning were excluded from morphometric analysis, 4. twenty cells per region per animal were analyzed, unless stated otherwise.

2.6 | Image processing

In order to extract geometrical and morphological information, trinary cell silhouettes were generated from each single microglia image by an (semi-) automated dual thresholding process (Figure 1d,e); first, a global threshold was applied on the single cell image resulting in segmentation of the cell from the image background. Then, a second threshold value was applied on the same image to identify and isolate the cell perikaryon (i.e., cell soma). Superimposition of both thresholds and subsequent processing resulted in three-color cell silhouette images in which the cell soma, the cell branches and the image background could be distinguished. All threshold steps were automated in a user-friendly tool (*MiaThreshold*, Windows/iOS) and minor adjustments to the cell silhouette - such as connecting pieces of the same branch (Figure 1d, asterisks) or adjusting the cell soma border (Figure 1d, closed triangles) - were facilitated by increasing or decreasing local threshold levels during the image conversion process. The single cell images were processed sequentially. Threshold levels were optimized manually for each single cell image. Detailed information on the thresholding steps can be found in Supplementary Figure 1a,b.

Then, fully connected branch skeletons of one-pixel thickness were automatically generated by repeated thinning of the cell silhouettes (Figure 1f). After complete thinning, the cell skeletons were processed in six consecutive automated steps to label branch start points (*start nodes*), branch crossings (*junctions*) and branch endings (*end nodes*) in each cell skeleton (for detailed information see Supplementary Figure 1c). Cell skeleton pixels that coincided with the cell soma region were excluded, restricting the cell skeletonization to the branch areas only.

2.7 | Automated feature extraction

Both cell silhouettes and cell skeletons were subjected to a fully automated morphometric analysis (*MiaCompute*, Windows/iOS). Microglia morphometrics included the quantification of 27 geometrical and morphological features, a Sholl analysis of the cell skeleton, and fractal

analyses of the cell surface area and cell perimeter, respectively (see Supplementary Figure 2 for list and definitions).

From the cell silhouette the following base morphometric features were extracted: pixel counts of the *soma area*, *soma perimeter*, *branch area*, *branch perimeter*, *cell area*, *cell perimeter*, *convex area* and *convex perimeter*. Ratios or 'form factors' such as *cell solidity*, *cell convexity*, *cell circularity* and *convex circularity* were calculated from these base features.

Morphometric features extracted from the cell skeleton included pixel counts of the branch skeleton (= *total branch length*) and total counts of branch *start nodes*, *junctions* and *end nodes*, respectively. Here, the number of start nodes is a measure for the number of primary branches of a cell. The '*end-to-start node ratio*' is a measure for the branching complexity, similar to the Schoenen ramification index (Schoenen, 1982) or ramification factor (Soltys et al., 2001). Pixels were converted to micrometers based on the pixel/μm resolution of the input images. In addition, the Euclidian distances of all nodes to the soma centroid were calculated for each cell skeleton. The feature '*cell spread*' is defined as the average Euclidian distance of all end nodes to the soma centroid.

2.8 | Sholl analysis

For Sholl analysis (Sholl, 1953), two-hundred concentric circles with a line thickness of one pixel and a step-size of two pixels were superimposed on each cell skeleton, with the soma centroid as center point. Subsequently, the number of intersections of the cell skeleton with each concentric circle was determined and plotted. Distances in pixels were converted to micrometers. The morphometric features *Sholl min*, *Sholl peak*, *Sholl peak intersections*, *Sholl max* and *Sholl sum* were extracted from the Sholl analysis results (see Supplementary Figure 2 for definitions). In addition, the *branching index* - a Sholl analysis-derived feature originally developed to describe neurite morphology (Garcia-Segura & Perez-Marquez, 2014) - was calculated for each cell.

2.9 | Fractal analyses

Two separate fractal methods were applied to determine the *fractal dimension* and *lacunarity* of the cell silhouettes. The *fractal dimension* of the cell perimeter is a measure for its 'roughness', while *lacunarity* of the cell surface area is a measure for its degree of structural variance (Smith Jr. et al., 1996). Both features have been used previously as discriminators for neuron and glia cell morphology (discussed in (Karperien et al., 2013; Smith Jr. et al., 1996)). To determine the *fractal dimension*, eleven counting grids with box sizes of 1×1 to 64×64 pixels were placed sequentially on the cell perimeter image. For each grid, all boxes with at least one cell perimeter pixel were counted (= box count). The logarithm of the box counts and respective box sizes were plotted on a log–log scale. The fractal dimension was defined as the absolute value of the slope for the linear regression of this function.

Lacunarity of the cell surface area was determined using a sliding box method. First, an axis-aligned minimum bounding box was

constructed around the cell silhouette. Then, eleven counting boxes with dimensions of 1×1 to 64×64 pixels were sequentially placed in the top left corner of the bounding box and moved in steps of one pixel over the entire bounding box region. At each sliding step, the number of cell area pixels within the counting box was determined ($=$ box mass). For each box size, the mean value and standard deviation of the histogram was determined. Here, *lacunarity* was defined as the mean coefficient of variation squared over all box sizes (Smith Jr. et al., 1996).

2.10 | Dimensionality reduction and HCPC

Prior to clustering, each feature dataset was normalized accordingly to ensure close-to-normal distribution ($-0.5 \leq$ skewness ≤ 0.5), followed by a Z-transform to scale and center the data ($\mu = 0$, SD $= 1$). Features that are summations of other features in the dataset (i.e., *cell area*, *cell perimeter* and *nodes*) were excluded from the PCA to reduce redundancy. For similar reasons, *Sholl sum* was excluded as this feature is reflected in the *total branch length* of the cell skeleton.

A PCA was applied on the remaining 23 morphometric features and PCs with an eigenvalue >1 were retained for clustering. Agglomerative hierarchical clustering on PCs was performed following Ward's method (Ward, 1963). Determination of the appropriate number of clusters was aided by visual inspection of the cell silhouettes within each cluster and by statistical comparison of morphometric features between clusters. The percentages of microglia per cluster were determined for each CNS region and subsequently compared to determine the distribution of microglia morphotypes over the 16 specified CNS regions. All pre-processing steps – including normalization and PCA – and HCPC were performed in R version 4.0.3.

2.11 | Cell density and nearest neighbor distance measurements

Microglia densities in the OBg, OBp, CPg, CA, DG, FIM, CC, TH, CTX, CBg, CBm, MO, SCg and SCw were determined by tagging and counting of all IBA1-positive somata in a specified region of interest (ROI) of known dimensions using the cell_counter.jar plugin (https://imagej.nih.gov/ij/plugins/cell-counter.html) for FIJI (Schindelin et al., 2012), with one ROI per animal and $n = 6$ animals per CNS region, unless mentioned otherwise. The spatial distribution of microglia in each ROI was determined by measuring the nearest neighbor distances – that is, the Euclidian distances between nearest cell somata - using the Nnd.class plugin for FIJI (developed by Yuxiong Mao). Nearest neighbor distances were averaged per ROI and then averaged per CNS region.

2.12 | Statistics

To statistically compare morphometric features between male (and female) CNS regions, separate linear mixed-effects models were fitted

per feature for each pairwise comparison, with 'region' as fixed effect and 'animal ID' as random effect to take into account that multiple cells were measured per animal per region. Likewise, for male/female comparisons per CNS region, models were fitted for each region with 'sex' as fixed effect and 'animal ID' as random effect. Statistical comparisons between CNS regions (or between sexes per CNS region) were assessed in R by means of Wald χ^2 tests using the anova.lme function of the nlme library. All *p*-values were adjusted for multiple testing following the Benjamini-Hochberg (false discovery rate, FDR) procedure (Benjamini & Hochberg, 1995).

Multiple pairwise comparisons of cell densities and nearest neighbor distances between male (and female) CNS regions were performed by means of a Kruskal-Wallis test followed by a Wilcoxon rank sum test (IBM SPSS statistics 26). The same approach was applied for statistical comparisons of morphometric features between cell clusters after HCPC. *p*-values were adjusted for multiple testing following the Benjamini-Hochberg (FDR) procedure (Benjamini & Hochberg, 1995).

2.13 | Computational tools and data availability

CellSelector, *MiaThreshold* and *MiaCompute* and the HCPC R-pipeline (*BRAT*) were constructed at the department of Biomedical Sciences of Cells and Systems, section Molecular Neurobiology of the University Medical Center Groningen, The Netherlands. The computational tools, as well as the data that support the findings of this study, are available from the corresponding author upon reasonable request.

3 | RESULTS

3.1 | Quantitative differences in microglia densities in the adult C57BL/6J CNS

To assess microglia heterogeneity in 3-month-old C57BL/6J mice, CNS tissues were collected and microglia were visualized by IBA1-immunohistochemistry. Sixteen white and gray matter regions along the rostro-caudal axis of the mouse CNS were analyzed for microglia density and morphology using our morphometrics pipeline (see Figure 1). Regional variations in the size and shape of microglia were apparent by eye, and the spatial distribution of microglia over the CNS parenchyma varied per region (Figure 2a). For example, microglia in the olfactory bulb and cortex were elaborately branched and densely packed, while cells in the cerebellum and medulla were less branched and sparsely distributed. To quantify the spatial distribution of microglia in the various regions, we determined the number of IBA1-positive cells per squared millimeter (Figure 2b), and the average nearest neighbor distances between cell somata for each region (Figure 2c.). Microglia cell densities (mean+/-SD) were highest in the anterior regions of the CTX ($183+/-53$), CP ($186+/-33$) and OBg ($162+/-16$), closely followed by the OBp ($150+/-33$) and medial regions DG ($153+/-29$), CA ($154+/-50$) and TH ($149+/-22$).

Similar cell densities were found in the white matter regions CC (154+/−50) and FIM (152+/−68). No significant differences in the average cell densities were found between these regions (see Data S1 for statistics). Note that variations in cell densities were high for several regions. The average distances between cells in aforementioned CNS regions were also comparable, ranging on average from 48 to
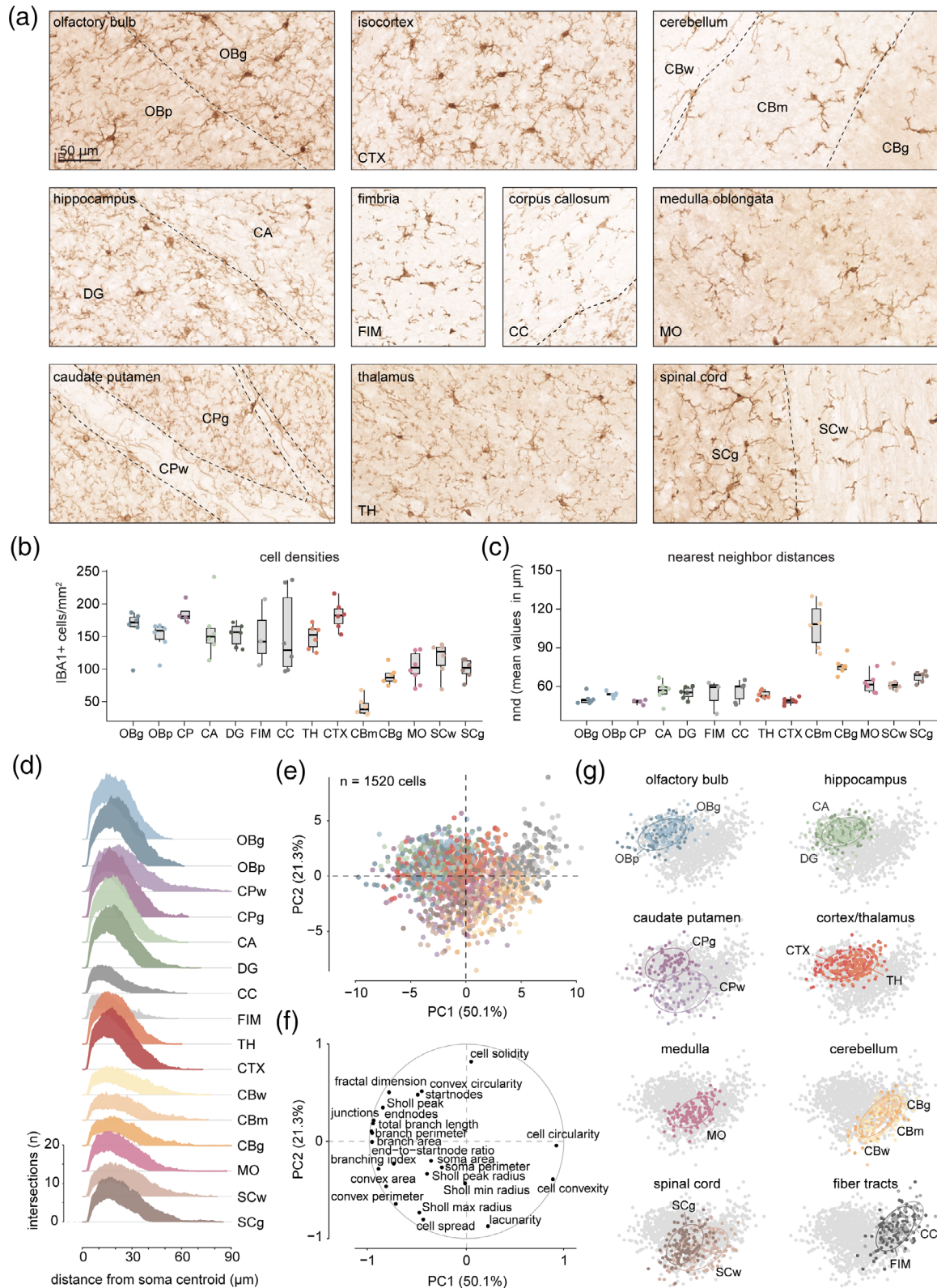

FIGURE 2 Legend on next page.

56 μm between cell somata (Figure 2b, see Data S1 for statistics). Microglia densities in the posterior regions were significantly lower; CBm 43+/−32, CBg 90+/−8, MO 104+/−22, SCw 116+/−31 and SCg 100+/−10 cells/mm² (Figure 2b). Interestingly, cells in these regions were also distributed more spatially, ranging on average from 108 μm between cell somata in CBm, to 76 μm in CBg, 62 μm in MO, 63 μm in SCw and 67 μm in SCg, respectively (Figure 2c).

3.2 | Morphological heterogeneity in microglia in adult male C57BL/6J CNS regions

Next, we extracted 1520 individual images of microglia from the slide scans of IBA1-immunostained male C57BL/6J brain and spinal cord samples and applied our newly developed morphometrics pipeline to determine the variation and extent of different microglial morphologies in these regions. The single cell images were converted to cell silhouette images and subjected to automated skeletonization and subsequent Sholl analysis, fractal analyses and extraction of 27 morphometric features (for feature definitions see Supplementary Figure 2).

Overall heterogeneity in microglia morphology in and between the various CNS regions was evident as determined by Sholl analysis (Figure 2d). Microglia in the anterior (OBg, OBp, CPg and CTX) and medial (CA, DG, TH) gray matter regions had on average a maximum cell radius of 40.6–44.0 μm (= Sholl max radius) and displayed the highest degree of branching complexity. Average cell radii of microglia in the TH, MO and SCg were comparable and ranged from 40.6 to 43.4 μm, however the branching complexity was lower when compared to OBg, OBp, CPg and CTX. Average cell radii for microglia in the internal capsule tracts (CPw, 56.5 μm) and white matter regions of the cerebellum (CBw, 56.4 μm) and spinal cord (SPw, 50.2 μm) were the largest of all regions investigated, with low branching complexity when compared to cells in other regions. Microglia in the white matter tracts CC and FIM were relatively the smallest cells with an average cell radius of 33.0 and 27.5 μm respectively and displayed on average the lowest branching complexity.

A comprehensive overview of the feature extraction dataset can be found in Supplementary Figure 3, and statistical comparisons between CNS regions for all features can be found in the Data S1. The features covered a broad selection of descriptors for soma size, cell size, area coverage, branching intensity and overall shape complexity. Similarities as well as statistical differences in microglia size and shape between CNS regions were evident. To facilitate interpretation of the feature dataset, the data was subjected to PCA (Figure 2e–g). Four features were excluded from the PCA to reduce redundancy as described in the material and methods. The distribution of all cell coordinates on the first component plane (PC1–PC2) was visualized (Figure 2e) and the contribution of the most prominent features to the first two PCs was determined (Figure 2f). In the first component (PC1) separation of microglia was mainly affected by 'roundness' of the cells (cell circularity and convex circularity; Figure 2f, right on the PC1-axis) and several equally contributing size and shape features in the opposite direction (Figure 2f, left on the PC1-axis). PC2 predominantly discriminated cells based on cell radius (Sholl max radius, cell spread) and cell 'compactness' (lacunarity vs. cell solidity; Figure 2f, PC2-axis). Microglia from the same CNS region grouped together, and each region overlapped to a certain extent with other CNS regions (Figure 2g). For example, cell coordinates for the olfactory bulb (OBg, OBp) and hippocampus (CA, DG) largely overlapped, suggesting that microglia populations in these regions are relatively similar in shape, size and/or branching complexity (Figure 2g, top). Cell coordinates for CPg, TH and CTX only partially overlapped with aforementioned regions, indicating that the microglia populations in these regions had less similar morphologies.

Cell coordinates for the medulla (MO) segregated from the anterior CNS regions and largely overlapped with the spinal cord gray matter (SCg) and to a certain degree with cell coordinates for the internal capsule tracts (CPw). Cerebellar cells also segregated and to some extent overlapped with cells from the spinal cord white matter (SCw) on one side and with white matter cells from the fimbria (FIM) and corpus callosum (CC) on the other side (Figure 2g, bottom). Taken together, these findings corroborate that microglia differ morphologically between CNS regions and that – based on the partial overlap between regions - most CNS regions contain multiple, overlapping morphological microglia subtypes.

FIGURE 2 Regional differences in density, size and shape of microglia in the adult male C57BL/6J mouse CNS. (a) Images of IBA1+ microglia in the olfactory bulb (OBg/OBp), isocortex, cerebellum (CBw/CBm/CBg), hippocampus (CA/DG), fimbria, corpus callosum, medulla oblongata, caudate putamen (CPg/CPw), thalamus (TH) and spinal cord (SCg/SCw) in 3-month old male C57BL/6J CNS. (b) Microglia cell densities and (c) the average nearest neighbor distances (nnd) between microglia in 16 select CNS regions. Upper, middle and lower hinges of the boxplots represent the first, second (= median) and third quantiles, respectively. Each dot represents one animal. (d) Sholl analysis ridge line plot for all CNS regions analyzed. Each line plot represents mean values +/-SD with n = 120 cells per CNS region, except OBg/OBp (n = 90 cells), CPw (n = 68 cells), CPg (n = 72 cells) and FIM/CBg/CBm/CBw (n = 60 cells). (e) PCA score plot for all cell coordinates on the first principal component plane (PC1/PC2) based on 23 morphometric features per cell. Each dot represents a cell. Colors indicate CNS regions. Numbers between brackets represent the variance retained by each PC. (f) Corresponding PCA loading plot, depicting the correlations between morphometric features and the first two components (PC1/PC2). (g) Same PCA plots as in panel (e), but now with each CNS region highlighted separately. Closed lines represent the 95% interval ellipses of each CNS region. Colors represent CNS regions. CA, cornu ammonis; CBg, cerebellum, granule cell layer; CBm, cerebellum, molecular layer; CBw, cerebellum, white matter; CC, corpus callosum; CPg, caudate putamen, gray matter; CPw, caudate putamen, internal capsule tracts; CTX, isocortex; DG, dentate gyrus; FIM, fimbria; MO, medulla oblongata; OBg, olfactory bulb, granule cell layer; OBp, olfactory bulb, plexiform/glomerular layer; SCg, spinal cord; SCw, spinal cord, white matter; TH, thalamus.
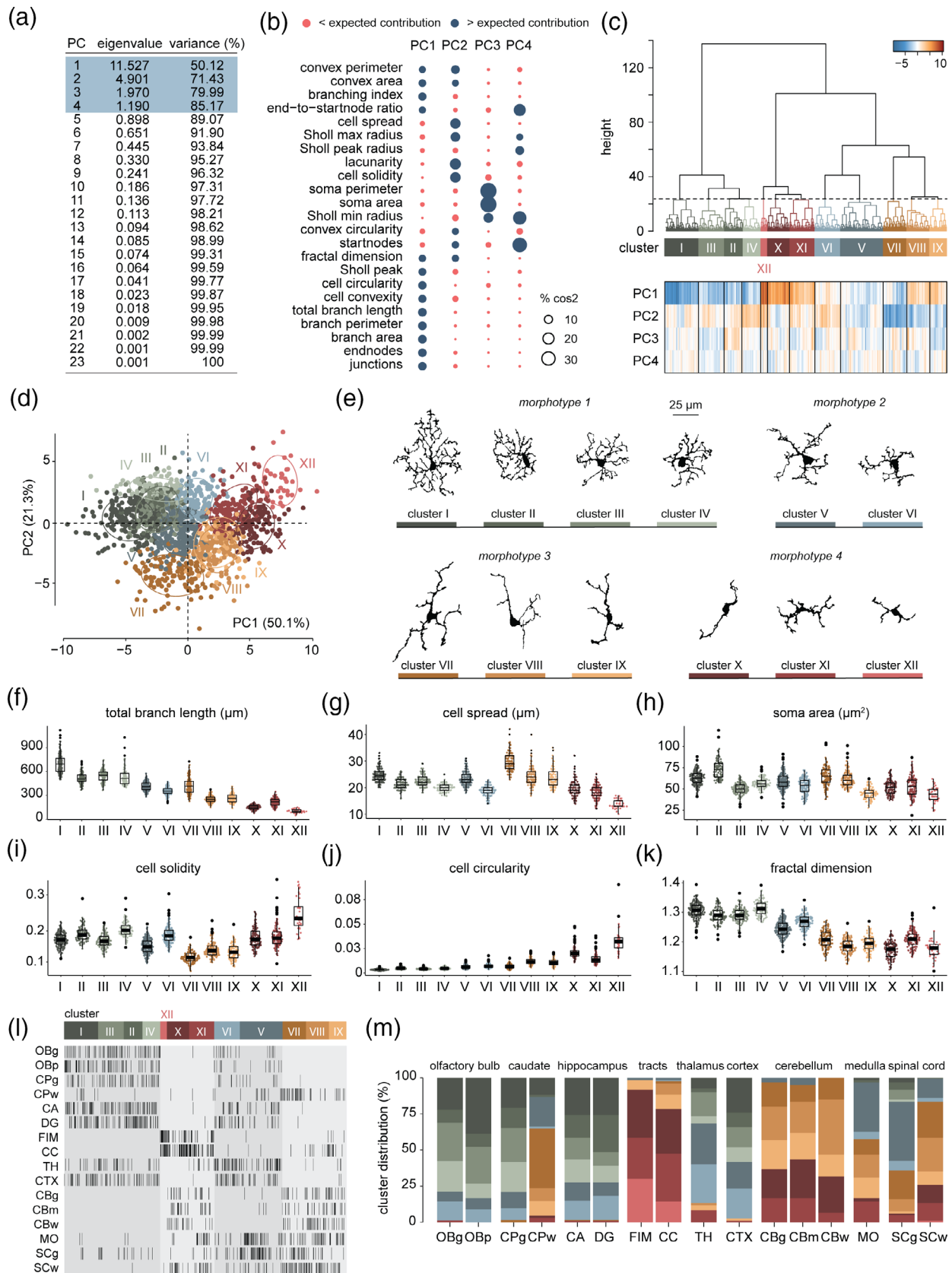
FIGURE 3 Legend on next page.

3.3 | HCPC-based categorization of microglia morphotypes in the adult male C57BL/6J CNS

To address the morphological heterogeneity in microglia in and between CNS regions, we identified microglia morphotypes in an unsupervised manner and compared the distribution of these morphotypes over the respective CNS regions. Identification and categorization of microglia morphotypes was achieved by means of HCPC. PCA lead to four PCs with an eigenvalue >1, accounting for 85.2% of the total variance observed in the dataset (Figure 3a). The contributions of the morphometric features to the first four PCs are depicted in Figure 3b. PC1 accounted for 50.1% of the observed variance and represented several equally contributing features; *convex perimeter*, *convex area*, *total branch length*, *branch perimeter*, *branch area*, *branching index*, *end-to-start node ratio*, *end nodes*, *junctions*, *Sholl peak*, *fractal dimension*, *cell circularity* and *cell convexity*. PC2 (21.3%) mainly represented variation in cell compactness (*cell solidity*, *lacunarity*), area size (*convex perimeter*, *convex area*), and cell radius (*cell spread*, *Sholl max radius*). PC3 (8.6%) predominantly represented variation in soma features *soma perimeter*, *soma area* and *Sholl min radius*. PC4 (5.2%) represented variation in the number of *start nodes*, and to a lesser extent the *end-to-start node ratio* and several Sholl features (*Sholl min radius*, *Sholl peak radius*, *Sholl max radius*).

Hierarchical clustering of the 1520 microglia based on the first four PCs resulted in twelve clusters, with each cluster representing a distinct microglia morphology (Figure 3c,d). PC1 and PC2 primarily contributed to the clustering of large to medium-sized microglia with elaborate secondary and tertiary branching (Figure 3e, morphotype 1; clusters I-IV in green), medium-sized microglia with elaborate but short secondary branching (morphotype 2; cluster V-VI in blue), large to medium-sized microglia with extended primary branching and sparse extended secondary branching (morphotype 3; clusters VII-IX in orange), and medium-sized to small compact cells with short primary branches with very limited secondary branching (morphotype 4; clusters X-XII in red). PC3 (and to some extent PC4) contributed to sub-clustering of these four morphotypes based on soma size and the degree of primary branching, further separating cluster II from III and cluster VIII from IX (not shown). A selection of morphometric features representing the morphological properties of microglia in clusters I-XII is depicted in Figure 3f–k.

3.4 | Distribution of microglia morphotypes along the rostro-caudal CNS axis in male C57BL/6J

To address the distribution of microglia morphotypes in the male C67BL/6 J CNS (Figure 3l), we determined the percentages of cells per cluster per CNS region and subsequently compared cluster distributions in and between regions along the rostro-caudal axis of the CNS (Figure 3m).

Cluster distributions in the gray matter regions OBg, OBp, CPg, CA and DG were highly comparable, with the majority of cells in clusters I-IV (morphotype 1; 72.5–83.3%) and to a lesser extent in clusters V-VI (morphotype 2; 16.7–25.8%). Although similar in the distribution of morphotypes, subtle variations between regions in microglia size, soma size and branching complexity were observed. Cells in clusters VII-IX and X-XII were rarely or not observed (<2%) in these regions. The majority of microglia in the CTX (>97%) and TH (>86%) were also categorized as morphotype 1 and 2. However, the distribution of cells over the clusters was more balanced in the CTX with 58.3% in clusters I-IV and 39.2% in clusters V-VI, respectively. Conversely, cells in the TH were primarily categorized in clusters V-VI (55%), followed by clusters I-IV (31.7%), clusters X-XII (8.3%) and clusters VII-IX (5%), respectively.

In contrast to microglia in the surrounding gray matter parenchyma, microglia aligned with the internal capsule tracts in the

FIGURE 3 Hierarchical clustering on principal components (HCPC) reveals distinct microglia morphotypes and their distribution in the CNS in 3-months old male C57BL/6J mice. (a) Table with the principal component (PC) eigenvalues and the cumulative variation retained in percentages for each consecutive PC. The first PCs with an eigenvalue >1 (PC1–PC4, indicated in blue) were retained for clustering. (b) The contribution of each morphometric feature to PC1–PC4, expressed as the *%cos²* (represented by dot size). Colors indicate values that are higher (blue) or lower (red) than the expected average contribution per PC. (c) Hierarchical clustering of 1520 IBA1+ cells based on PC1–PC4 yielded twelve distinct microglia clusters (I to XII), with cluster I ($n = 184$), II ($n = 101$), III ($n = 138$), IV ($n = 96$), V ($n = 231$), VI ($n = 138$), VII ($n = 126$), VIII ($n = 124$), IX ($n = 91$), X ($n = 120$), XI ($n = 135$), and XII ($n = 36$ cells), respectively. The horizontal axis of the dendrogram represents individual cells, the vertical axis represents the linkage distance defined as the squared Euclidian distance. The dashed horizontal line represents the cut-off for twelve clusters. The corresponding PC scores for each cell are plotted as vertical bars in the heatmap below the dendrogram. (d) PCA plot represents all cell coordinates (shown as dots) on the first two dimensional planes PC1/PC2. The percentage of variability retained in the respective PCs is stated between brackets on the x- and y-axes. Colors indicate cell clusters I to XII. The centroids of the 95% confidence ellipses represent the weighted centers of mass of each cell cluster. (e) Representative silhouette images of microglia in clusters I to XII, categorized per morphotype. Colors represent clusters. (f-k) Representative morphometric features for microglia in cluster I to XII. Depicted are (f) the total branch length, (g) cell spread, (h) soma area, (i) cell solidity, (j) cell circularity and (k) fractal dimension. Upper, middle and lower hinges of the boxplots represent the first, second (= median), and third quantiles, respectively. Each dot represents one cell, black dots represent outliers. Units on the y-axes are stated between brackets in the header of each plot. Roman numerals on the x-axes represent the cell clusters. (l) Distribution of all 1520 microglia over clusters I to XII, specified per CNS region. Each black vertical line represents one cell. (m) Stacked bars represent the mean percentages of microglia in clusters I to XII per CNS region. Colors represent clusters I to XII. CA, cornu ammonis; CBg, cerebellum, granule cell layer; CBm, cerebellum, molecular layer; CBw, cerebellum, white matter; CC, corpus callosum; CPg, caudate putamen, gray matter; CPw, caudate putamen, internal capsule tracts; CTX, isocortex; DG, dentate gyrus; FIM, fimbria; MO, medulla oblongata; OBg, olfactory bulb, granule cell layer; OBp, olfactory bulb, plexiform/glomerular layer; SCg, spinal cord; SCw, spinal cord, white matter; TH, thalamus.

caudate putamen (CPw) mainly consisted of morphotype 3 cells (clusters VII-IX, 64.7%). The majority of these cells were categorized in cluster VII (60.3%), that is, relatively large bipolar cells with long primary processes and sporadic secondary branching.

Microglia in the white matter tracts FIM and CC mainly consisted of morphotype 4 cells (clusters X-XII; 91.7% and 78.3%, respectively), that is, small microglia with basic and short primary branching. The CC contained on average more cells with morphotype 3 (clusters VII-IX; 19.2%) than the FIM (6.7%).

Cerebellar microglia were predominantly categorized in clusters VII-IX (morphotype 3; CBg: 60%, CBm: 51.2%, CBw: 68.3%) and clusters X-XII (morphotype 4; CBg: 36.7%, CBm: 43.3%, CBw: 31.7%). Note that the cluster distributions in gray and white matter cerebellum were highly comparable.

Microglia morphotypes in the gray matter regions of the medulla (MO) and spinal cord (SCg) were heterogeneously distributed. Microglia in the MO were evenly distributed over clusters V-VI (morphotype 2; 39.2%) and clusters VII-IX (morphotype 3; 40.8%) and, to a lesser extent, over clusters X-XI (morphotype 4; 16.7%) and clusters I-IV (morphotype 1; 3.3%). The distribution of microglia morphotypes in the SCg was similarly heterogeneous with 47.5% of the cells in clusters V-VI (morphotype 2), 30% in clusters VII-IX (morphotype 3), 16.7% in clusters I-IV (morphotype 1) and 5.8% in clusters X-XII (morphotype 4). In contrast to SCg, microglia in SCw mainly consisted of morphotype 3 (clusters VII-IX; 57.5%), followed by morphotype 4 (clusters X-XII; 25.8%) and morphotype 2 (clusters V-VI; 15.83%). Morphotype 1 was rarely observed in the SCw (clusters I-IV; <0.9%).

Interestingly, microglia bordering the internal capsule tracts displayed distinct polar morphologies with complex side-branching in the caudate gray matter but smooth elongated branching along the tracts (Supplemental Figure 5a/b). Similarly, hippocampal microglia projecting into the stratum granulosum (DG) or stratum pyramidale (CA) displayed polar morphologies with elaborate secondary and tertiary branching into the neuronal fiber layers, but plain elongated branching into the granule (DG) and pyramidal (CA) cell layers (Supplemental Figure 5c/d), suggesting that local cues regulate microglia morphology.

3.5 | No differences in microglia morphotypes or their distribution in adult male and female C57BL/6J CNS

Finally, we combined the male and female feature datasets to compare the regional distribution of CNS microglia morphotypes between sexes (Figure 4). Single cell images of in total 3041 microglia from 16 specified CNS regions in male (1520 cells) and female (1521 cells) C57BL/6J littermates (derived from $n = 7$ animals per group) were grouped and subjected to morphometrics and subsequent categorization by means of HCPC. The first PCs with an eigenvalue >1 (here, PC1–PC4) were retained for clustering, yielding twelve clusters (Figure 4a/b). Representative cell silhouettes and Sholl curves for each cluster are shown in Figure 4c,d, respectively. The same morphotypes

as described for the male dataset were identified in the combined male–female dataset; microglia in clusters I-IV shared the same morphotype, that is, multiple primary branches with elaborate secondary and tertiary branching (morphotype 1), but differed in size (cluster I > II > III > IV), area coverage (cluster I > II/III > IV), soma size (cluster I/II > III/IV) and branching complexity (cluster I > III > II > IV). Morphotype 1 was predominantly found in the anterior and medial gray matter areas. Microglia in clusters V and VI had lower numbers of primary branches with abundant and short secondary branching (morphotype 2). Differences between cells in clusters V and VI concerned cell size (*cell area*, *total branch length*), soma size (*soma area/perimeter*) and the number of primary branches (*start nodes*, cluster V > VI in all cases). Microglia in clusters VII-IX had relatively low numbers of elongated primary branches (low number of *start nodes*, large *cell spread*) with limited or no secondary branching (low number of *junctions*, high *lacunarity*, low *cell solidity*; morphotype 3). Differences between clusters VII-IX were mainly based on cell size and the degree of secondary branching (cluster VII > VII > IX in both cases). Morphotype 3 was mainly found in microglia in white matter regions and posterior gray matter regions. Microglia in clusters X-XII were relatively the smallest cells with short primary branching and limited secondary branching (morphotype 4). This morphotype was predominantly found in the fimbria, corpus callosum and cerebellar white matter. Differences between cell clusters X-XII were predominantly based on average soma size (cluster XI > X > XII), compactness (cluster X > XI > XII) and overall branching complexity (cluster X > XI > XII).

The regional distributions of the various microglia morphologies (cell clusters I-XII) were determined, as well as the average Sholl curves per CNS region, and were subsequently compared between sexes (Figure 4e). In short, no differences in the regional distribution of microglia morphotypes, nor in the average Sholl curves per region were found between males and females. To corroborate these findings, we statistically compared all morphometric features per CNS region for males and females; out of 432 comparisons only two features in one region were found to be significant between sexes ($p < .05$), namely *cell convexity* and *cell circularity* in the OBp.

Finally, we compared for each CNS region the cell densities and nearest neighbor distances between males and females (Supplemental Figure 4). No statistical differences between sexes in either cell density or nearest neighbor distances were found at any CNS region (for statistics see Data S1). Summarizing, microglia morphotypes and their distribution in the adult male and female C57BL/6J mouse CNS are in essence indistinguishable.

4 | DISCUSSION

4.1 | Regional heterogeneity in microglia morphotypes in the adult mouse CNS

Microglia are morphologically diverse and heterogeneously distributed over the CNS. Subtle variations in microglia morphotypes were observed in each CNS compartment. Here, we identified four general
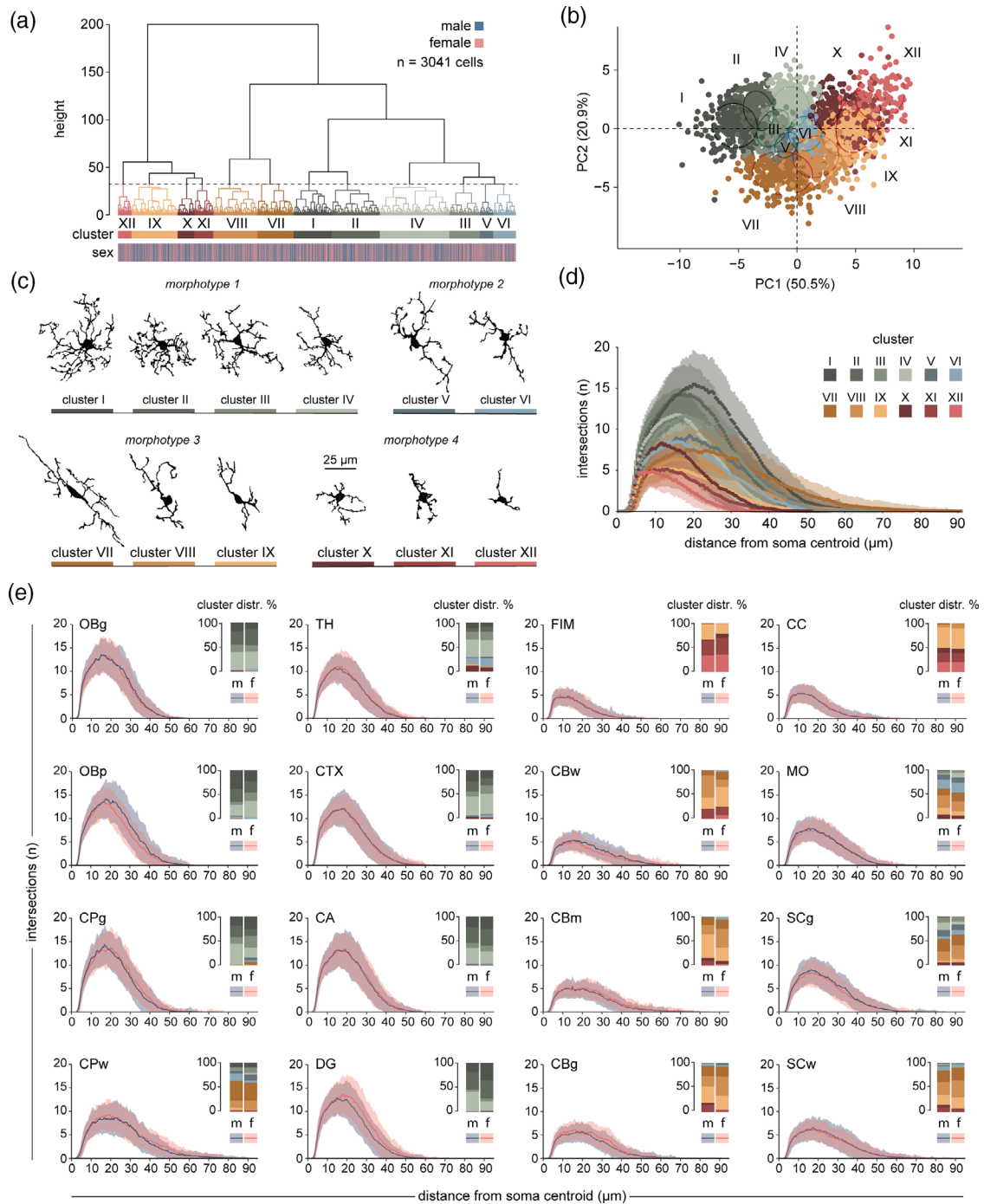
FIGURE 4 Comparison of CNS microglia morphotypes and their distribution in the CNS in 3-months old male and female C57BL/6J littermates. (a) Hierarchical clustering of in total 3041 yielded twelve clusters (I to XII), with cluster I ($n = 292$), II ($n = 367$), III ($n = 233$), IV ($n = 533$), V ($n = 102$), VI ($n = 169$), VII ($n = 278$), VIII ($n = 338$), IX ($n = 353$), X ($n = 127$), XI ($n = 145$), and XII ($n = 104$ cells), respectively. Vertical lines on the horizontal axis of the dendrogram represent individual cells, the vertical axis represents the linkage distance defined as the squared Euclidian distance ($=$ height). The dashed horizontal line represents the cut-off for twelve clusters. Colors indicate clusters. Vertical lines in the lower horizontal bar represent cells from males (in blue) and females (in red), respectively. (b) PCA plot represents all cell coordinates (shown as dots) on the first two dimensional planes PC1/PC2. Colors indicate cell clusters I to XII. The centroids of the 95% confidence ellipses represent the weighted centers of mass of each cluster. The percentages of variability retained for PC1 and PC2 are stated between brackets on the x- and y-axes. (c) Representative silhouette images of microglia in clusters I to XII, categorized per morphotype. (d) Sholl plots for clusters I to XII. Each colored line represents one cluster (mean $+/-$ SD). (e) Cluster distribution plots (stacked bars, colors indicate clusters) and Sholl line plots (mean values $+/-$ SD, colors indicate sexes) for male and female C57BL/6J littermates in 16 specified CNS regions. CA, cornu ammonis; CBg, cerebellum, granule cell layer; CBm, cerebellum, molecular layer; CBw, cerebellum, white matter; CC, corpus callosum; CPg, caudate putamen, gray matter; CPw, caudate putamen, internal capsule tracts; CTX, isocortex; DG, dentate gyrus; FIM, fimbria; MO, medulla oblongata; OBg, olfactory bulb, granule cell layer; OBp, olfactory bulb, plexiform/glomerular layer; SCg, spinal cord; SCw, spinal cord, white matter; TH, thalamus.

morphotypes in the adult mouse CNS in the sixteen regions we have investigated, and each morphotype could be subdivided into smaller sub-clusters of microglia of similar shape that varied in soma size, cell size and/or branching intensity. Anterior and medial gray matter regions shared the same microglia morphotypes: (1) radial cells with high secondary/tertiary branching and (2) radial cells with high but short secondary branching, however subtle differences in the distributions of these morphotypes existed between regions. Notably, these moderate differences between regions were only found by HCPC and not by morphometrics or Sholl analysis, underscoring the advantage of a clustering approach over basic morphometrics.

Microglia morphotypes in white matter regions were distinct from those in gray matter regions, with either longitudinally branched microglia with long primary branches and few elongated secondary branches (morphotype 3) and/or small(er) cells with short primary branching with sparse secondary branching (morphotype 4). Also here, subtle differences in microglia size and branching intensity were observed between white matter regions. Posterior regions such as the medulla oblongata and the spinal cord gray matter contained a mix of gray and white matter morphotypes (predominantly type 2 and 3), with the majority of microglia being radially or longitudinally branched with relatively sparse secondary branching. Microglia aligning the internal capsule tracts in the caudate putamen were on average the largest longitudinally branched cells. Microglia morphologies in the cerebellar white and gray matter regions were highly comparable but distinct from other regions, and the distributions of microglia morphotypes over the respective cerebellar layers were indistinguishable.

Microglial densities differed between CNS compartments. Microglia in the anterior and medial gray and white matter regions were less spaced than microglia in the posterior regions cerebellum, medulla and spinal cord. The average distance between neighboring microglia was highest in the cerebellum, medulla and spinal cord, respectively. Cell densities in the cerebellum were the lowest of all regions investigated, with CBm < CBg. Similar findings were previously reported for adult BALB/C mice (Lawson et al., 1990), C57BL/6 mice (Colombo et al., 2022; Vela et al., 1995) and adult rat (Savchenko et al., 2000) using various staining protocols. Microglial densities in the cortex, cerebellum and other gray matter regions are distinct but highly conserved in mammalian species (Dos Santos et al., 2020). Interestingly, microglia constitute approximately 7%–9% of all non-neuronal cells in most CNS regions, while the spatial distribution differs per region. Nonetheless, studies in rat cortex have shown that although the spatial distribution of microglia differs between the various cortical layers, microglia morphology is consistent (Kongsui et al., 2014). In line with these findings, we observed that the distribution of microglial morphotypes in the cerebellum was equal across layers, although microglial densities differed (Figure 2b,c, see also Vela et al., (1995)). It is therefore likely that the variation in microglia morphology across CNS regions and their spatial distribution are independent properties.

The morphology of a microglial cell is most likely dictated by its microenvironment and affected by differences in local environmental cues. In recent years, a plethora of external and internal cues have been identified that can either stimulate microglia, ameliorate their

response, or retain microglia in a surveilling ramified state (reviewed in Biber et al., (2007); Galea et al., (2007)). In this context, various secreted factors and membrane-membrane interactions with other cell-types have been identified that (partially) regulate microglial function and hence often microglial morphology. Of note, the relation between microglial function and morphology is still rather elusive. Drastic changes in local cues, such as an invading pathogen or cell death, induce profound changes in microglia. However, several studies have reported overlapping gene expression profiles in ramified and amoeboid microglia, suggesting that morphological changes are not always necessarily accompanied by altered gene activity (reviewed in Paolicelli et al. (2022); Tan et al. (2020)).

Note that in this study sagittal sections were analyzed, allowing us to capture and analyze microglia from most CNS regions in one rostro-caudal plane. In some CNS compartments, microglial branches may be oriented in a particular direction, which is especially the case for microglia aligning the white matter tracts of the FIM, CC and internal capsule (CPw). Depending on the orientation, the tracts run either perpendicular or parallel to the sectioning plane, which may affect the 'view' of microglial morphologies in these regions. It is possible that a coronal or transverse tissue orientation could result in subtle differences in the morphological categorization outcome. Similarly, tissue thickness is an important factor when analyzing microglial morphology. Tissue sections of 50–100 μm may capture the full span of microglial branching, but analyses are often performed on two dimensional images of maximum z-stack projections that thus overrepresent microglial arborization. To minimize mesh-like overrepresentation of the branching, we have investigated microglial cross sections with a limited z-axis distance of 16 μm, thereby capturing the branching shape more closely.

4.2 | No sexual dimorphism in microglia in the adult mouse CNS

We detected no statistical differences in the spatial distribution of microglia between adult male and female littermates in the CNS regions investigated. In addition, the distribution of microglia morphotypes was remarkably comparable between both sexes in all regions. Even at the most detailed level, when comparing all morphometric features per CNS region between both sexes, only 2 out of the 432 feature comparisons were significant in just one of the 16 regions investigated (OBp, _cell convexity_ and _cell circularity_). These data indicated that, by and large, microglia in adult male and female mice are morphometrically indistinguishable.

A recent study by Colombo et al. using a topological data analysis approach with bootstrapped persistent images to morphologically describe heterogeneous microglia populations in male and female mouse CNS reported sexual dimorphism in microglia in adult C57BL/6J cerebellum, cochlear nucleus, substantia nigra, primary somatosensory cortex and olfactory bulb, but not in the frontal cortex and dentate gyrus (Colombo et al., 2022). Differences in microglial heterogeneity between sexes were subtle at an adult age and more

prominent during development and degeneration. Unfortunately, in the study of Colombo et al. sexual dimorphism in adult animals could not be recapitulated by morphometric analysis alone (i.e., no differences were found), complicating direct comparison with our findings. Another study by Guneykaya et al. (Guneykaya et al., 2018) reported statistical differences in microglial numbers and average soma size in the cortex, hippocampus and amygdala in coronal sections of adult male and female C57BL/6J mice, which is not in agreement with our findings and those of Colombo et al. Taken together, these results have to be interpreted with care. Differences in tissue orientation, section thickness, analytical models and statistical approaches could to some extent explain the differences in reported findings.

4.3 | A pipeline for microglia morphometrics and objective morphological categorization

Here, we provide a user-friendly pipeline for single cell image segmentation, automated microglia morphometrics and objective categorization of microglia in IBA1-immunostained histological sections. Our studies underline the current opinion that, although classical microglia morphometrics provides elaborate and detailed information on microglia size and shape, it is not sufficient to identify and discriminate microglial subtypes in a morphologically heterogenous population. We have shown here that clustering on PCs provides an effective approach to morphotype microglia without the need for relevant feature selection (see also Heng et al., (2021); Kater et al., (2023); Zhang et al., (2021)). The sensitivity of our pipeline was demonstrated by its ability to identify microglia subtypes across sixteen CNS regions, both white and gray matter, and its ability to detect even subtle differences in microglia morphotype distributions between CNS regions. Taken together, our pipeline provides valuable means to resolve identification and categorization of microglia morphotypes in any CNS region or (disease) model.

AUTHOR CONTRIBUTIONS

Hilmar R.J. van Weering: conceptualization (equal), methodology design (equal), investigation (lead), formal analysis (lead), visualization and writing original draft (lead). **Tjalling W. Nijboer:** conceptualization (equal), methodology development and design (equal), software (equal). **Maaike L. Brummer:** data curation (supporting), methodology design and development (equal), formal analysis (supporting), software (equal). **Erik W.G. M. Boddeke:** review and editing (supporting). **Bart J.L. Eggen:** writing original draft (supporting), review and editing (supporting).

ORCID

Hilmar R. J. van Weering https://orcid.org/0009-0003-2243-2605
Erik W. G. M. Boddeke https://orcid.org/0000-0002-5058-9648
Bart J. L. Eggen https://orcid.org/0000-0001-8941-0353

REFERENCES

Benjamini, Y., & Hochberg, Y. (1995). Controlling the false discovery rate: A practical and powerful approach to multiple testing. *Journal of the Royal Statistical Society: Series B: Methodological*, *57*(1), 289–300. https://doi.org/10.1111/j.2517-6161.1995.tb02031.x

Biber, K., Neumann, H., Inoue, K., & Boddeke, H. W. (2007). Neuronal 'On' and 'Off' signals control microglia. *Trends in Neurosciences*, *30*(11), 596–602. https://doi.org/10.1016/j.tins.2007.08.007

Bottcher, C., Schlickeiser, S., Sneeboer, M. A. M., Kunkel, D., Knop, A., Paza, E., Fidzinski, P., Kraus, L., Snijders, G. J. L., Kahn, R. S., Schulz, A. R., Mei, H. E., Psy, N. B. B., Hol, E. M., Siegmund, B., Glauben, R., Spruth, E. J., de Witte, L. D., & Priller, J. (2019). Human microglia regional heterogeneity and phenotypes determined by multiplexed single-cell mass cytometry. *Nature Neuroscience*, *22*(1), 78–90. https://doi.org/10.1038/s41593-018-0290-2

Colombo, G., Cubero, R. J. A., Kanari, L., Venturino, A., Schulz, R., Scolamiero, M., Agerberg, J., Mathys, H., Tsai, L. H., Chacholski, W., Hess, K., & Siegert, S. (2022). A tool for mapping microglial morphology, morphOMICs, reveals brain-region and sex-dependent phenotypes. *Nature Neuroscience*, *25*(10), 1379–1393. https://doi.org/10.1038/s41593-022-01167-6

Davalos, D., Grutzendler, J., Yang, G., Kim, J. V., Zuo, Y., Jung, S., Littman, D. R., Dustin, M. L., & Gan, W. B. (2005). ATP mediates rapid microglial response to local brain injury in vivo. *Nature Neuroscience*, *8*(6), 752–758. https://doi.org/10.1038/nn1472

de Sousa, A. A., Dos Reis, R. R., de Lima, C. M., de Oliveira, M. A., Fernandes, T. N., Gomes, G. F., Diniz, D. G., Magalhaes, N. M., Diniz, C. G., Sosthenes, M. C., Bento-Torres, J., Diniz, J. A., Jr., Vasconcelos, P. F., & Diniz, C. W. (2015). Three-dimensional morphometric analysis of microglial changes in a mouse model of virus encephalitis: Age and environmental influences. *The European Journal of Neuroscience*, *42*(4), 2036–2050. https://doi.org/10.1111/ejn.12951

Dos Santos, S. E., Medeiros, M., Porfirio, J., Tavares, W., Pessoa, L., Grinberg, L., Leite, R. E. P., Ferretti-Rebustini, R. E. L., Suemoto, C. K., Filho, W. J., Noctor, S. C., Sherwood, C. C., Kaas, J. H., Manger, P. R., & Herculano-Houzel, S. (2020). Similar microglial cell densities across brain structures and mammalian species: Implications for brain tissue function. *The Journal of Neuroscience*, *40*(24), 4622–4643. https://doi.org/10.1523/JNEUROSCI.2339-19.2020

Eggen, B. J. L., Boddeke, E., & Kooistra, S. M. (2019). Regulation of microglia identity from an epigenetic and transcriptomic point of view. *Neuroscience*, *405*, 3–13. https://doi.org/10.1016/j.neuroscience.2017.12.010

Fernandez-Arjona, M. D. M., Grondona, J. M., Granados-Duran, P., Fernandez-Llebrez, P., & Lopez-Avalos, M. D. (2017). Microglia morphological categorization in a rat model of neuroinflammation by hierarchical cluster and principal components analysis. *Frontiers in Cellular Neuroscience*, *11*, 235. https://doi.org/10.3389/fncel.2017.00235

Galea, I., Bechmann, I., & Perry, V. H. (2007). What is immune privilege (not)? *Trends in Immunology*, 28(1), 12–18. https://doi.org/10.1016/j.it.2006.11.004

Garcia-Segura, L. M., & Perez-Marquez, J. (2014, Apr 15). A new mathematical function to evaluate neuronal morphology using the Sholl analysis. *Journal of Neuroscience Methods*, 226, 103–109. https://doi.org/10.1016/j.jneumeth.2014.01.016

Grabert, K., & McColl, B. W. (2018). Isolation and phenotyping of adult mouse microglial cells. *Methods in Molecular Biology*, 1784, 77–86. https://doi.org/10.1007/978-1-4939-7837-3_7

Grabert, K., Michoel, T., Karavolos, M. H., Clohisey, S., Baillie, J. K., Stevens, M. P., Freeman, T. C., Summers, K. M., & McColl, B. W. (2016). Microglial brain region-dependent diversity and selective regional sensitivities to aging. *Nature Neuroscience*, 19(3), 504–516. https://doi.org/10.1038/nn.4222

Guneykaya, D., Ivanov, A., Hernandez, D. P., Haage, V., Wojtas, B., Meyer, N., Maricos, M., Jordan, P., Buonfiglioli, A., Gielniewski, B., Ochocka, N., Comert, C., Friedrich, C., Artiles, L. S., Kaminska, B., Mertins, P., Beule, D., Kettenmann, H., & Wolf, S. A. (2018, Sep 4). Transcriptional and translational differences of microglia from male and female brains. *Cell Reports*, 24(10), 2773–2783 e2776. https://doi.org/10.1016/j.celrep.2018.08.001

Gzielo, K., Soltys, Z., Rajfur, Z., & Setkowicz, Z. K. (2019, Aug 10). The impact of the ketogenic diet on glial cells morphology. A Quantitative Morphological Analysis. *Neuroscience*, 413, 239–251. https://doi.org/10.1016/j.neuroscience.2019.06.009

Heindl, S., Gesierich, B., Benakis, C., Llovera, G., Duering, M., & Liesz, A. (2018). Automated morphological analysis of microglia after stroke. *Frontiers in Cellular Neuroscience*, 12, 106. https://doi.org/10.3389/fncel.2018.00106

Heng, Y., Zhang, X., Borggrewe, M., van Weering, H. R. J., Brummer, M. L., Nijboer, T. W., Joosten, L. A. B., Netea, M. G., Boddeke, E., Laman, J. D., & Eggen, B. J. L. (2021, Feb 22). Systemic administration of beta-glucan induces immune training in microglia. *Journal of Neuroinflammation*, 18(1), 57. https://doi.org/10.1186/s12974-021-02103-4

Karperien, A., Ahammer, H., & Jelinek, H. F. (2013). Quantitating the subtleties of microglial morphology with fractal analysis. *Frontiers in Cellular Neuroscience*, 7, 3. https://doi.org/10.3389/fncel.2013.00003

Kater, M. S. J., Huffels, C. F. M., Oshima, T., Renckens, N. S., Middeldorp, J., Boddeke, E., Smit, A. B., Eggen, B. J. L., Hol, E. M., & Verheijen, M. H. G. (2023). Prevention of microgliosis halts early memory loss in a mouse model of Alzheimer's disease. *Brain, Behavior, and Immunity*, 107, 225–241. https://doi.org/10.1016/j.bbi.2022.10.009

Kongsui, R., Beynon, S. B., Johnson, S. J., & Walker, F. R. (2014). Quantitative assessment of microglial morphology and density reveals remarkable consistency in the distribution and morphology of cells within the healthy prefrontal cortex of the rat. *Journal of Neuroinflammation*, 11, 182. https://doi.org/10.1186/s12974-014-0182-7

Kreutzberg, G. W. (1996). Microglia: A sensor for pathological events in the CNS. *Trends in Neurosciences*, 19(8), 312–318. https://doi.org/10.1016/0166-2236(96)10049-7

Lawson, L. J., Perry, V. H., Dri, P., & Gordon, S. (1990). Heterogeneity in the distribution and morphology of microglia in the normal adult mouse brain. *Neuroscience*, 39(1), 151–170. https://doi.org/10.1016/0306-4522(90)90229-w

Leyh, J., Paeschke, S., Mages, B., Michalski, D., Nowicki, M., Bechmann, I., & Winter, K. (2021). Classification of microglial morphological phenotypes using machine learning. *Frontiers in Cellular Neuroscience*, 15, 701673. https://doi.org/10.3389/fncel.2021.701673

Masuda, T., Sankowski, R., Staszewski, O., Bottcher, C., Amann, L., Sagar, Scheiwe, C., Nessler, S., Kunz, P., van Loo, G., Coenen, V. A., Reinacher, P. C., Michel, A., Sure, U., Gold, R., Grun, D., Priller, J., Stadelmann, C., & Prinz, M. (2019). Spatial and temporal heterogeneity of mouse and human microglia at single-cell resolution. *Nature*, 566(7744), 388–392. https://doi.org/10.1038/s41586-019-0924-x

Masuda, T., Sankowski, R., Staszewski, O., & Prinz, M. (2020). Microglia heterogeneity in the single-cell era. *Cell Reports*, 30(5), 1271–1281. https://doi.org/10.1016/j.celrep.2020.01.010

Nimmerjahn, A., Kirchhoff, F., & Helmchen, F. (2005). Resting microglial cells are highly dynamic surveillants of brain parenchyma in vivo. *Science*, 308(5726), 1314–1318. https://doi.org/10.1126/science.1110647

Ohgomori, T., Yamada, J., Takeuchi, H., Kadomatsu, K., & Jinno, S. (2016). Comparative morphometric analysis of microglia in the spinal cord of SOD1(G93A) transgenic mouse model of amyotrophic lateral sclerosis. *The European Journal of Neuroscience*, 43(10), 1340–1351. https://doi.org/10.1111/ejn.13227

Paolicelli, R. C., Sierra, A., Stevens, B., Tremblay, M. E., Aguzzi, A., Ajami, B., Amit, I., Audinat, E., Bechmann, I., Bennett, M., Bennett, F., Bessis, A., Biber, K., Bilbo, S., Blurton-Jones, M., Boddeke, E., Brites, D., Brone, B., Brown, G. C., ... Wyss-Coray, T. (2022, Nov 2). Microglia states and nomenclature: A field at its crossroads. *Neuron*, 110(21), 3458–3483. https://doi.org/10.1016/j.neuron.2022.10.020

Salamanca, L., Mechawar, N., Murai, K. K., Balling, R., Bouvier, D. S., & Skupin, A. (2019). MIC-MAC: An automated pipeline for high-throughput characterization and classification of three-dimensional microglia morphologies in mouse and human postmortem brain samples. *Glia*, 67(8), 1496–1509. https://doi.org/10.1002/glia.23623

Savchenko, V. L., McKanna, J. A., Nikonenko, I. R., & Skibo, G. G. (2000). Microglia and astrocytes in the adult rat brain: Comparative immunocytochemical analysis demonstrates the efficacy of lipocortin 1 immunoreactivity. *Neuroscience*, 96(1), 195–203. https://doi.org/10.1016/s0306-4522(99)00538-2

Schindelin, J., Arganda-Carreras, I., Frise, E., Kaynig, V., Longair, M., Pietzsch, T., Preibisch, S., Rueden, C., Saalfeld, S., Schmid, B., Tinevez, J. Y., White, D. J., Hartenstein, V., Eliceiri, K., Tomancak, P., & Cardona, A. (2012). Fiji: An open-source platform for biological-image analysis. *Nature Methods*, 9(7), 676–682. https://doi.org/10.1038/nmeth.2019

Schoenen, J. (1982). The dendritic organization of the human spinal cord: The dorsal horn. *Neuroscience*, 7(9), 2057–2087. https://doi.org/10.1016/0306-4522(82)90120-8

Schweitzer, L., & Renehan, W. E. (1997). The use of cluster analysis for cell typing. *Brain Research. Brain Research Protocols*, 1(1), 100–108. https://doi.org/10.1016/s1385-299x(96)00014-1

Sholl, D. A. (1953). Dendritic organization in the neurons of the visual and motor cortices of the cat. *Journal of Anatomy*, 87(4), 387–406 https://www.ncbi.nlm.nih.gov/pubmed/13117757

Smith, T. G., Jr., Lange, G. D., & Marks, W. B. (1996). Fractal methods and results in cellular morphology-dimensions, lacunarity and multifractals. *Journal of Neuroscience Methods*, 69(2), 123–136. https://doi.org/10.1016/S0165-0270(96)00080-5

Soltys, Z., Orzylowska-Sliwinska, O., Zaremba, M., Orlowski, D., Piechota, M., Fiedorowicz, A., Janeczko, K., & Oderfeld-Nowak, B. (2005). Quantitative morphological study of microglial cells in the ischemic rat brain using principal component analysis. *Journal of Neuroscience Methods*, 146(1), 50–60. https://doi.org/10.1016/j.jneumeth.2005.01.009

Soltys, Z., Ziaja, M., Pawlinski, R., Setkowicz, Z., & Janeczko, K. (2001, Jan 1). Morphology of reactive microglia in the injured cerebral cortex. Fractal analysis and complementary quantitative methods. *Journal of Neuroscience Research*, 63(1), 90–97. https://doi.org/10.1002/1097-4547(20010101)63:1<90::AID-JNR11>3.0.CO;2-9

Stetzik, L., Mercado, G., Smith, L., George, S., Quansah, E., Luda, K., Schulz, E., Meyerdirk, L., Lindquist, A., Bergsma, A., Jones, R. G., Brundin, L., Henderson, M. X., Pospisilik, J. A., & Brundin, P. (2022). A novel automated morphological analysis of Iba1+ microglia using a deep learning assisted model. *Frontiers in Cellular Neuroscience*, 16, 944875. https://doi.org/10.3389/fncel.2022.944875

Tan, Y. L., Yuan, Y., & Tian, L. (2020). Microglial regional heterogeneity and its role in the brain. *Molecular Psychiatry*, *25*(2), 351–367. https://doi.org/10.1038/s41380-019-0609-8

Vela, J. M., Dalmau, I., Gonzalez, B., & Castellano, B. (1995). Morphology and distribution of microglial cells in the young and adult mouse cerebellum. *The Journal of Comparative Neurology*, *361*(4), 602–616. https://doi.org/10.1002/cne.903610405

Verdonk, F., Roux, P., Flamant, P., Fiette, L., Bozza, F. A., Simard, S., Lemaire, M., Plaud, B., Shorte, S. L., Sharshar, T., Chretien, F., & Danckaert, A. (2016). Phenotypic clustering: A novel method for microglial morphology analysis. *Journal of Neuroinflammation*, *13*(1), 153. https://doi.org/10.1186/s12974-016-0614-7

Wake, H., Moorhouse, A. J., Jinno, S., Kohsaka, S., & Nabekura, J. (2009, Apr 1). Resting microglia directly monitor the functional state of synapses in vivo and determine the fate of ischemic terminals. *The Journal of Neuroscience*, *29*(13), 3974–3980. https://doi.org/10.1523/JNEUROSCI.4363-08.2009

Ward, J. H. (1963). Hierarchical grouping to optimize an objective function. *Journal of the American Statistical Association*, *58*, 236–244.

Yamada, J., & Jinno, S. (2013). Novel objective classification of reactive microglia following hypoglossal axotomy using hierarchical cluster analysis. *The Journal of Comparative Neurology*, *521*(5), 1184–1201. https://doi.org/10.1002/cne.23228

Zhang, X., Heng, Y., Kooistra, S. M., van Weering, H. R. J., Brummer, M. L., Gerrits, E., Wesseling, E. M., Brouwer, N., Nijboer, T. W., Dubbelaar, M. L., Boddeke, E., & Eggen, B. J. L. (2021). Intrinsic DNA damage repair deficiency results in progressive microglia loss and replacement. *Glia*, *69*(3), 729–745. https://doi.org/10.1002/glia.23925

SUPPORTING INFORMATION

Additional supporting information can be found online in the Supporting Information section at the end of this article.

How to cite this article: van Weering, H. R. J., Nijboer, T. W., Brummer, M. L., Boddeke, E. W. G. M., & Eggen, B. J. L. (2023). Microglia morphotyping in the adult mouse CNS using hierarchical clustering on principal components reveals regional heterogeneity but no sexual dimorphism. *Glia*, *71*(10), 2356–2371. https://doi.org/10.1002/glia.24427